High-Order ENO Schemes for Unstructured Meshes Based on Least-Squares Reconstruction

Carl F. Ollivier-Gooch*
Mathematics and Computer Science Division
Argonne National Laboratory

1 Introduction

High-order accurate schemes for conservation laws for unstructured meshes are not nearly so well advanced as such schemes for structured meshes. Consequently, little or nothing is known about the possible practical advantages of high-order discretization on unstructured meshes. This article is part of an ongoing effort to develop high-order schemes for unstructured meshes to the point where meaningful information can be obtained about the trade-offs involved in using spatial discretizations of higher than second-order accuracy on unstructured meshes.

This article describes a high-order accurate ENO reconstruction scheme, called DD-L_2-ENO, for use with vertex-centered upwind flow solution algorithms on unstructured meshes. The solution of conservation equations in this context can be broken naturally into three phases:

1. **Solution reconstruction**, in which a polynomial approximation of the solution is obtained in each control volume.

2. **Flux integration** around each control volume, using an appropriate flux function and a quadrature rule with accuracy commensurate with that of the reconstruction.

3. **Time evolution**, which may be implicit, explicit, multigrid, or some hybrid.

This article focuses primarily on solution reconstruction. A new high-order ENO reconstruction

technique for unstructured meshes is presented. The scheme is uniformly accurate for smooth functions, even near extrema. Near discontinuities, the scheme gracefully reduces the order of accuracy to control overshoots. Because the scheme is based on least-squares reconstruction, implementation on unstructured meshes is straightforward. Finally, the present scheme has better convergence behavior than stencil-searching ENO schemes because the ENO property is obtained by the use of weights which vary smoothly with the data rather than by switching.

Section 2 summarizes of existing reconstruction techniques. Section 3 discusses the new reconstruction scheme, with some attention given to implementation details. Section 4 gives examples of the capabilities of the reconstruction scheme. Section 5 discusses a number of technical points concerning construction of a flow solver compatible with the new scheme. Section 6 gives several example solutions to the Euler equations. Finally, Section 7 gives some conclusions from the present work and discusses some issues still remaining for high-order accurate solution of the Euler equations on unstructured meshes.

2 Overview of Reconstruction Techniques

The use of high-order spatial discretization on structured meshes is commonplace. The development of MUSCL schemes [1] focused on attaining high-order accuracy for smooth solutions, with a drop in accuracy near discontinuities and near extrema in the solution. More recently, essentially non-oscillatory (ENO) schemes have been developed to ensure uniformly high-order accuracy for all points with a smooth neighborhood. Early work in one dimension [2, 3, 4] demonstrated the feasibility of this reconstruction scheme, which searches for the smoothest stencil for reconstruction in each control volume. Extensions to multiple space dimensions soon fol-

lowed [5, 6, 7, 8].

Stencil-searching ENO schemes share the problem that small changes in the solution from time step to time step causes stencil "switching" and prevents convergence to a numerical steady-state. This problem has recently been addressed by a new family of weighted ENO (WENO) schemes [9, 10]. These schemes use a weighted sum of all possible stencils rather than searching for the smoothest possible stencil. Stencils containing non-smooth data are not excluded by theses schemes, but instead are given weights on the order of truncation error. Because the weights vary smoothly with the data, these schemes should converge well (although we are unaware of any studies of this issue). These schemes are one dimensional and are applied direction-by-direction for reconstruction on multidimensional structured meshes.

Several extensions of ENO schemes to unstructured meshes have been made based on stencil-searching approaches [11, 12]. These schemes, like their structured-mesh counterparts, are guaranteed to reconstruct based on smooth data when this is possible. They have the same convergence difficulties as structured stencil-searching schemes.

A more common approach to reconstruction on unstructured meshes is to use least-squares reconstruction followed by some limiting procedure to eliminate overshoots [13, 14].* The reconstruction scheme described here is an extension of previous work [16] on the use of data-dependent least-squares reconstruction to produce ENO schemes. Previously, high-order reconstruction was demonstrated in one dimension, and second-order reconstruction and flow solutions were shown in two dimensions. The present work discusses high-order reconstruction and flow solution in two dimensions. The reconstruction scheme uses a fixed stencil similar to that used by a typical k-exact least-squares scheme. An initial data-independent least-squares reconstruction is computed, and the smoothness of the data on the stencil is inferred from the results. Data-dependent weights are applied to the least-squares problem to virtually eliminate the influence of non-smooth data, and a data-dependent reconstruction is computed. As in WENO schemes, the data-dependent weights are chosen to satisfy the ENO property of Liu, Osher, and Chan [9].

An important difference between the present scheme and WENO schemes is their behavior when a smooth stencil does not exist. Where enough smooth data exists — near a single discontinuity or boundary,

---

*Similar in intent are SLIP schemes [15], which are closely related to FCT schemes. SLIP schemes are local extremum diminishing and can in principle be extended to higher than second-order accuracy.

for example — each scheme reconstructs to the nominal order of accuracy. Where there are not enough smoothly connected neighbors, the scheme automatically reduces the order of accuracy of the reconstruction locally rather than contaminating the reconstruction. The result is a reconstruction scheme that is well behaved near multiple discontinuities while retaining high-order accuracy elsewhere.

3 Data-dependent Least-Squares Reconstruction

Consider a domain Ω that has been tessellated; the tessellation has a characteristic length scale Δx, at least locally. The median dual of the tessellation defines for each vertex v_i a surrounding control volume V_i. For any function $u(\vec{x})$ defined on Ω and its control-volume averaged values $\overline{u}_i$, the DD-L_2-ENO will compute an expansion $R_i(\vec{x} - \vec{x}_i)$ about v_i that

- conserves the mean;

- has compact support;

- reconstructs exactly polynomials of degree $\leq k$ (equivalently, $R_i(\vec{x} - \vec{x}_i) - u(\vec{x}) = \mathcal{O}\left(\Delta x^{k+1}\right)$); and

- satisfies the ENO property of Liu, Osher, and Chan [9].

The remainder of this section describes this process in two dimensions. Reduction to one dimension, extension to three dimensions, and application to structured meshes are all straightforward variations on the theme.

3.1 Conservation of the Mean

Conservation of the mean within a control volume requires that

$$\int_{V_i} R_i(\vec{x} - \vec{x}_i)dA = \int_{V_i} u(\vec{x})dA. \qquad (1)$$

This can be accomplished by using zero-mean polynomials in expanding about v_i, that is, by writing

$$\begin{aligned}
R_i(\vec{x} - \vec{x}_i) &= \overline{u}_i + \left.\frac{\partial u}{\partial x}\right|_i (x - x_i - \overline{x}_i) \\
&+ \left.\frac{\partial u}{\partial y}\right|_i (y - y_i - \overline{y}_i) \\
&+ \left.\frac{\partial^2 u}{\partial x^2}\right|_i \frac{(x - x_i)^2 - \overline{x^2}_i}{2}
\end{aligned}$$

$$+ \left.\frac{\partial^2 u}{\partial x \partial y}\right|_i \left((x - x_i)(y - y_i) - \overline{xy}_i\right)$$

$$+ \left.\frac{\partial^2 u}{\partial y^2}\right|_i \frac{(y - y_i)^2 - \overline{y^2}_i}{2} + \cdots \quad (2)$$

, where

$$\overline{x^n y^m}_i \equiv \frac{1}{A_i} \int_{V_i} (x - x_i)^n (y - y_i)^m dA. \quad (3)$$

By inspection, the expansion of Equation 2 satisfies Equation 1. As a practical matter, the integral of Equation 3 is most easily computed by using Green's theorem to convert it to a boundary integral around V_i.

$$\overline{x^n y^m} = \frac{1}{(n + 1)A_i} \int_{\partial V_i} (x - x_i)^{n+1} (y - y_i)^m dy \quad (4)$$

This integral may be evaluated exactly by using a Gaussian quadrature of appropriate order along the boundary of the control volume.

3.2 Compact Support

Compact support implies that the reconstruction R_i will only use data from a stencil $\{V_j\}_i$ whose members are both physically near $\vec{x}_i$ and topologically near control volume i. The size of the compact stencil is determined by the number of required derivatives. In practice, including additional neighbors allows leeway for ignoring some non-smooth data while retaining high-order accurate reconstruction. The use of 3, 8, and 14 neighbors for second-, third-, and fourth-order accuracy (to compute 2, 5, and 9 derivatives, respectively) seems to be sufficient.

Stencils are determined iteratively. The initial stencil consists of first vertex neighbors. For control volumes that need a larger stencil, second vertex neighbors are added. Additional layers of neighbors are added until a large enough stencil has been found for each control volume; this process is illustrated in Figure 1. Nearly all interior points use first neighbors for second order and add second neighbors for third and fourth order. Boundary points often add another layer of neighbors. Stencils are computed in a pre-processing step and stored for later use.

3.3 Accuracy for Smooth Functions

Accuracy of a reconstruction for smooth functions can be stated in two equivalent ways. The reconstruction can be said to be k-exact for some k if, when reconstructing $P(\vec{x}) \epsilon \{x^m y^n : m + n \leq k\}$ from control volume averages,

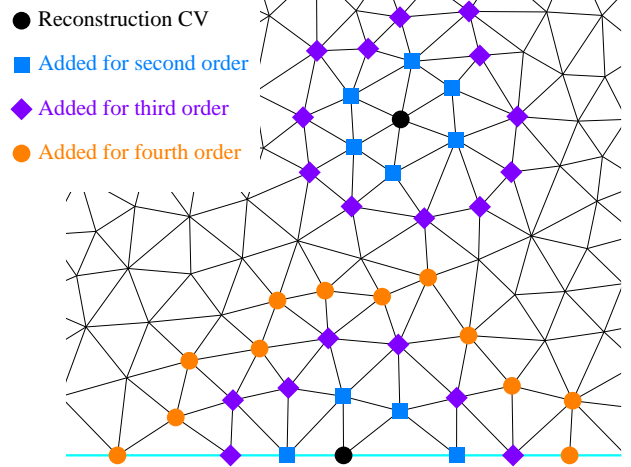$$R_i(\vec{x} - \vec{x}_i) \equiv P(\vec{x}). \quad (5)$$

Figure 1: Reconstruction Stencils for DD-L_2-ENO

Equivalently, when reconstructing a general function $u(\vec{x})$ from control volume averages,

$$R_i(\vec{x} - \vec{x}_i) = u(\vec{x}) + \mathcal{O}\left(\Delta x^{k+1}\right). \quad (6)$$

In practice, this accuracy requirement means that the modified Taylor series expansion of R_i given in Equation 2 must be carried out through the kth derivatives. To compute these derivatives, we seek to minimize the error in predicting the mean value of the function for control volumes in the stencil $\{V_j\}_i$. The error for a single control volume is given by

$$E_{j,i} = \frac{1}{A_j} \int_{V_j} R_i(\vec{x} - \vec{x}_i) dA - \overline{u}_j. \quad (7)$$

Because this integral can be expressed in terms of geometric quantities and approximations to derivatives of u at $\vec{x}_i$, the errors $E_{j,i}$ can be used to formulate a least-squares problem for the derivatives. The remainder of this subsection develops this formulation in detail.

The mean value, for a single control volume V_j, of the reconstructed function R_i is

$$\frac{1}{A_j} \int_{V_j} R_i(\vec{x} - \vec{x}_i) dA = \overline{u}_i \quad (8)$$

$$+ \left.\frac{\partial u}{\partial x}\right|_i \left(\frac{1}{A_j} \int_{V_j} (x - x_i) dA - \overline{x}_i\right)$$

$$+ \left.\frac{\partial u}{\partial y}\right|_i \left(\frac{1}{A_j} \int_{V_j} (y - y_i) dA - \overline{y}_i\right)$$

$$+ \left.\frac{\partial^2 u}{\partial x^2}\right|_i \left(\frac{1}{2A_j} \int_{V_j} (x - x_i)^2 dA - \frac{1}{2}\overline{x^2}_i\right)$$

$$+ \left.\frac{\partial^2 u}{\partial x \partial y}\right|_i \left(\frac{1}{A_j} \int_{V_j} (x - x_i)(y - y_i) dA - \overline{xy}_i\right)$$

$$+ \left. \frac{\partial^2 u}{\partial y^2} \right|_i \left(\frac{1}{2 A_j} \int_{V_j} (y - y_i)^2 dA - \frac{1}{2} \overline{y^2}_i \right) + \cdots$$

To avoid computing moments of each control volume in $\{V_j\}_i$ about v_i, replace $x - x_i$ and $y - y_i$ with $(x - x_j) + (x_j - x_i)$ and $(y - y_j) + (y_j - y_i)$, respectively. Expanding and integrating, we obtain

$$\frac{1}{A_j} \int_{V_j} R_i(\vec{x} - \vec{x}_i) = \overline{u}_i + \left. \frac{\partial u}{\partial x} \right|_i (\overline{x}_j + (x_j - x_i) - \overline{x}_i)$$

$$+ \left. \frac{\partial u}{\partial y} \right|_i (\overline{y}_j + (y_j - y_i) - \overline{y}_i)$$

$$+ \left. \frac{\partial^2 u}{\partial x^2} \right|_i \frac{\overline{x^2}_j + 2\overline{x}_j(x_j - x_i) - (x_j - x_i)^2 - \overline{x^2}_i}{2}$$

$$+ \left. \frac{\partial^2 u}{\partial x \partial y} \right|_i (\overline{xy}_j + \overline{x}_j(y_j - y_i) + (x_j - x_i)\overline{y}_j$$

$$+ (x_j - x_i)(y_j - y_i) - \overline{xy}_i)$$

$$+ \left. \frac{\partial^2 u}{\partial y^2} \right|_i \frac{\overline{y^2}_j + 2\overline{y}_j(y_j - y_i) - (y_j - y_i)^2 - \overline{y^2}_i}{2}$$

$$+ \cdots. \tag{9}$$

The geometric terms in this equation are of the general form

$$\widehat{x^n y^m}_{ij} \equiv \frac{1}{A_j} \int_{V_j} ((x - x_j) + (x_j - x_i))^n$$

$$\cdot ((y - y_j) + (y_j - y_i))^m dA - \overline{x^n y^m}_i$$

$$= \sum_{l=0}^{m} \sum_{k=0}^{n} \binom{m}{l} \binom{n}{k} (x_j - x_i)^k$$

$$\cdot (y_j - y_i)^l \overline{x^{n-k} y^{m-l}}_j - \overline{x^n y^m}_i. \tag{10}$$

In these terms, we can write

$$\frac{1}{A_j} \int_{V_j} R_i(\vec{x} - \vec{x}_i) = \overline{u}_i + \left. \frac{\partial u}{\partial x} \right|_i \widehat{x}_{ij} + \left. \frac{\partial u}{\partial y} \right|_i \widehat{y}_{ij}$$

$$+ \left. \frac{\partial^2 u}{\partial x^2} \right|_i \frac{\widehat{x^2}_{ij}}{2} + \left. \frac{\partial^2 u}{\partial x \partial y} \right|_i \widehat{xy}_{ij} + \left. \frac{\partial^2 u}{\partial y^2} \right|_i \frac{\widehat{y^2}_{ij}}{2}$$

$$+ \cdots. \tag{11}$$

Equation 11 evaluates the mean value of the reconstruction $R_i(\vec{x} - \vec{x}_i)$ for a control volume j, given the low-order derivatives of the solution at v_i and low-order moments of the control volumes. With this in hand, we can easily write down a weighted least-squares problem for the derivatives.

$$\begin{bmatrix} L_{i1} \\ L_{i2} \\ L_{i3} \\ \vdots \\ L_{iN} \end{bmatrix} \begin{pmatrix} \frac{\partial u}{\partial x} \\ \frac{\partial u}{\partial y} \\ \frac{1}{2} \frac{\partial^2 u}{\partial x^2} \\ \frac{\partial^2 u}{\partial x \partial y} \\ \frac{1}{2} \frac{\partial^2 u}{\partial y^2} \\ \vdots \end{pmatrix}_i = \begin{pmatrix} w_{i1} (\overline{u}_1 - \overline{u}_i) \\ w_{i2} (\overline{u}_2 - \overline{u}_i) \\ w_{i3} (\overline{u}_3 - \overline{u}_i) \\ \vdots \\ w_{iN} (\overline{u}_N - \overline{u}_i) \end{pmatrix},$$

$$\tag{12}$$

where

$$L_{ij} = \left(w_{ij} \widehat{x}_{ij} \ \ w_{ij} \widehat{y}_{ij} \ \ w_{ij} \widehat{x^2}_{ij} \ \ w_{ij} \widehat{xy}_{ij} \ \ w_{ij} \widehat{y^2}_{ij} \ \ \cdots \right) \tag{13}$$

and

$$w_{ij} = \frac{1}{|\vec{x}_j - \vec{x}_i|^2}. \tag{14}$$

3.4 Solution of the Least-Squares Problem

In the present work, the least-squares problem of Equation 12 is solved by using Householder transformations to reduce the left-hand side of Equation 12 to upper-triangular form. After the upper triangularization is complete, back-substitution yields the required derivatives. There are several good reasons to use this approach instead of the simpler normal equation solution to the least-squares problem.

- Using Householder transformations gives a more accurate solution to the least-squares problem than using normal equations, especially for ill-conditioned matrices. The error in the solution is $\mathcal{O}(\epsilon K)$ using Householder transformations and $\mathcal{O}(\epsilon K^2)$ for normal equations, where K is the condition number of the non-square matrix and ϵ is machine precision [17]. This also implies greater robustness.

- As a further improvement in robustness, the Householder transform approach can detect singular and nearly singular matrices on the fly. If the least-squares problem is (nearly) singular, a column with (nearly) zero elements on and below the diagonal will be encountered during Householder triangularization. This failure occurs because the stencil is inadequate to support the requested number of derivatives. To resolve this, either more points must be added to the reconstruction stencil or the reconstruction must be modified to include fewer derivatives. The latter course is adopted in this work. Derivatives are computed only to the highest order for which *all*

derivatives can be computed; the additional incomplete set of derivatives is discarded, because no increase in order of accuracy is possible by retaining them.

- After the upper triangularization of the least-squares problem is complete, the residual for the solution is available at virtually no cost. Before back substitution, the problem looks like the following.

$$
\begin{bmatrix}
x & x & x & \cdots & x \\
  & x & x & \cdots & x \\
  &   & x & \cdots & x \\
  &   &   & \ddots & x \\
  &   &   &   & x \\
  & 0 &   &   &   \\
\end{bmatrix}
\begin{pmatrix}
\frac{\partial u}{\partial x} \\
\frac{\partial u}{\partial y} \\
\frac{1}{2}\frac{\partial^2 u}{\partial x^2} \\
\frac{\partial^2 u}{\partial x \partial y} \\
\frac{1}{2}\frac{\partial^2 u}{\partial y^2} \\
\vdots
\end{pmatrix}_i
=
\begin{pmatrix}
r_1 \\
r_2 \\
\vdots \\
r_m \\
r_{m+1} \\
\vdots \\
r_{n-1} \\
r_n
\end{pmatrix}
\tag{15}
$$

If we seek m derivatives using an n point stencil, the first m equations will be satisfied exactly. The remaining $n - m$ equations will not be; the residual $\hat{\mathcal{R}}$, which is the same as the residual for the original problem, is

$$
\hat{\mathcal{R}} = \sqrt{\sum_{l=m+1}^{n} r_l^2}.
\tag{16}
$$

Scaling this by the RMS value of the geometric weight removes local mesh scale effects:

$$
\mathcal{R} = \frac{\hat{\mathcal{R}}}{\sqrt{\sum w_{ij}^2 / n}}.
\tag{17}
$$

$\mathcal{R}$ has several uses. Within the context of this work, $\mathcal{R}$ will be used to compute data-dependent weightings. $\mathcal{R}$ also is a good measure of how well the solution is approximated locally, making it yet another candidate for use as a refinement measure.

3.5 Reconstruction of Non-smooth Functions

The reconstruction scheme described above is designed for smooth functions. For non-smooth functions — those with $\mathcal{O}(1)$ discontinuities — such a scheme allows overshoots of $\mathcal{O}(1)$. This is not desirable for either function approximation or scientific computation, where such overshoots can easily produce aphysical values. This problem has typically been addressed by performing a reconstruction

with geometric weights and preventing overshoots by heuristically *limiting*, or reducing, the derivatives (e.g., [13, 14]). While this approach is not unsuccessful, it provides only a mechanical solution to an underlying theoretical problem. Specifically, the stencil for a control volume i near a discontinuity will include control volumes j that lie on the opposite side of the discontinuity. Because the function is not smooth, approximating data in V_j by a modified Taylor series around v_i is inappropriate. Ignoring this mathematical fact causes the unphysically large derivatives that limiting seeks to reduce.

A better alternative is to reconstruct using only data that *is* smoothly connected to data in i. This approach is taken directly by ENO schemes, which by design search for a smooth stencil and completely exclude non-smooth data from the reconstruction. WENO schemes work less directly, using all possible stencils and weighting those containing non-smooth data with a weight that is of the order of the truncation error.

In the present weighted least-squares context, weights are assigned to control volumes rather than to stencils. Nevertheless, the goal is to weight non-smooth data with $\mathcal{O}(\Delta x^{k+1})$ to satisfy the ENO condition of Liu, Osher, and Chan [9]. We seek to construct a data-dependent weight that will multiply the previously calculated geometric weight. This construction is based on two observations.

1. If the function is non-smooth and the neighborhood of V_i crosses a discontinuity, then a modified Taylor expansion does not adequately describe the function locally and there will be one or more control volumes j for which

$$
\frac{1}{A_j} \int_{V_j} R_i(\vec{x} - \vec{x}_i) dA - \overline{u}_j = \mathcal{O}(1).
\tag{18}
$$

This means that the residual $\mathcal{R}$ of the least-squares problem will be $\mathcal{O}(1)$. On the other hand, for stencils that cover only smooth regions of the function,

$$
R_i(\vec{x} - \vec{x}_i) - u(\vec{x}) = \mathcal{O}(\Delta x^{k+1})
\tag{19}
$$

and $\mathcal{R}$ is also $\mathcal{O}(\Delta x^{k+1})$. Therefore, $\mathcal{R}$ can be used as a gauge of the smoothness of the data for the entire stencil $\{V_j\}_i$.

2. Whether the data in V_j is smoothly connected to data in V_i can be determined asymptotically by evaluating

$$
\frac{u_j - u_i}{|\vec{x}_j - \vec{x}_i|} = \begin{cases}
\mathcal{O}(1) & \text{smoothly connected} \\
\mathcal{O}(\Delta x^{-1}) & \text{not smoothly} \\
& \qquad \text{connected}
\end{cases}
\tag{20}
$$

We seek a data-dependent weighting that uses $\mathcal{R}$ to detect stencils with non-smooth data and $\frac{u_j - u_i}{|\vec{x}_j - \vec{x}_i|}$ to determine which data within that stencil should be excluded and which included. One appropriate weighting is

$$W_{ij}^{DD} = \frac{1}{1 + k\mathcal{R}\left|\frac{u_j - u_i}{|\vec{x}_j - \vec{x}_i|}\right|^{(k+1)}}, \qquad (21)$$

where $\mathcal{R}\left|\frac{u_j - u_i}{|\vec{x}_j - \vec{x}_i|}\right|^{(k+1)}$ is a smoothness indicator analogous to the divided difference indicators of [9, 10] but appropriate for unstructured meshes and least-squares reconstruction. $\mathcal{R}$ is computed from a data-independent least-squares reconstruction, as described above. We are concerned only with the asymptotic behavior of W_{ij}^{DD}, so the value of k is not critical; 0.1 seems to be a good choice.

Asymptotically, the behavior of this weighting for the three important cases is

$$W_{ij}^{DD} = \begin{cases} 1 + \mathcal{O}\left(\Delta x^{(k+1)}\right) & \text{smooth stencil} \\ \mathcal{O}\left(1\right) & \text{smooth data in stencil} \\ & \text{w/ nonsmooth data} \\ \mathcal{O}\left(\Delta x^{-(k+1)}\right) & \text{nonsmooth data} \end{cases}$$

$$(22)$$

That is, for stencils containing only smoothly connected data, the data-dependent weights are all approximately 1, ensuring that the good qualities of the data-independent reconstruction will be preserved for smooth functions. For stencils that are not entirely smooth, the data-dependent weight for non-smooth data is smaller than that for smooth data by a factor of the order of truncation error. These weightings satisfy the ENO condition of Liu, Osher, and Chan [9].

The data-dependent least-squares problem is closely related to the data-independent problem. The jth row in the least-squares problem of Equation 12 is modified by scaling with the data-dependent weight. With no further computation, the least-squares problem becomes

$$\begin{bmatrix} L'_{i1} \\ L'_{i2} \\ L'_{i3} \\ \vdots \\ L'_{iN} \end{bmatrix} \begin{pmatrix} \frac{\partial u}{\partial x} \\ \frac{\partial u}{\partial y} \\ \frac{1}{2}\frac{\partial^2 u}{\partial x^2} \\ \frac{\partial^2 u}{\partial x \partial y} \\ \frac{1}{2}\frac{\partial^2 u}{\partial y^2} \\ \vdots \end{pmatrix}_i = \begin{pmatrix} w'_{i1}\left(\overline{u}_1 - \overline{u}_i\right) \\ w'_{i2}\left(\overline{u}_2 - \overline{u}_i\right) \\ w'_{i3}\left(\overline{u}_3 - \overline{u}_i\right) \\ \vdots \\ w'_{iN}\left(\overline{u}_N - \overline{u}_i\right) \end{pmatrix} \quad (23)$$

where

$$L'_{ij} = \left(w'_{ij}\widehat{x}_{ij} \ \ w'_{ij}\widehat{y}_{ij} \ \ w'_{ij}\widehat{x^2}_{ij} \ \ w'_{ij}\widehat{xy}_{ij} \ \ w'_{ij}\widehat{y^2}_{ij} \ \ \cdots \right),$$

$$(24)$$

and

$$w'_{ij} = \frac{1}{|\vec{x}_j - \vec{x}_i|^2}W_{ij}^{DD}. \qquad (25)$$

As data-dependent weights are assigned, the number that are numerically large is counted. If too few control volumes are assigned high data-dependent weights, insufficient smoothly connected data is available to compute the desired number of derivatives.[†] Similar to the data-independent case, this results in a lowering of the nominal order of accuracy of the reconstruction locally. This loss of accuracy is most likely to occur for control volumes straddling discontinuities; near the intersection of two discontinuities; or near the impingement of a discontinuity on a boundary. Because no non-smooth data has a significant impact on the reconstruction, however, large overshoots in the reconstruction are not expected. This would not be true if non-smooth data were included.

In contrast, stencil-searching ENO schemes such as Abgrall's [12] can sometimes avoid local degradation of accuracy near a discontinuity by extending the stencil farther away from the discontinuity. However, for cases with medium resolution in which some control volumes do not have enough smoothly connected neighbors, stencil-searching schemes will use non-smooth (and therefore irrelevant) data. This approach can lead to large overshoots for such cases.

Also, consider a control volume V_i that is divided by a discontinuity and therefore has an averaged function value that lies between the values on either side of the discontinuity. Here, reconstruction makes little physical sense because no smoothly connected data exists. The present scheme can detect such a situation and choose to reconstruct the solution in V_i as piecewise constant, whereas stencil searching schemes will still seek a high-order polynomial reconstruction.

3.6 Summary

The data-dependent least-squares approach can be used to produce function reconstructions that satisfy the ENO condition. The least-squares heritage of these DD-L_2-ENO schemes allows them to be applied easily to function reconstruction on unstructured meshes in multiple dimensions. The algorithm can be summarized as follows:

- **Input.** A computational mesh, structured or unstructured.

  The average value of a function to be reconstructed for each control volume.

[†]Because data-dependent weights should all be $\mathcal{O}\left(()1\right)$ for smooth data, a cutoff value of 0.1 is used to determine whether a weight is "high".

- **Output.** An ENO reconstruction of the function, in the form of a modified Taylor series expansion about each vertex, valid within the control volume surrounding the vertex.

- **Preprocessing.** For each control volume V_i, find a sufficiently large set of nearby control volumes $\{V_j\}_i$ for reconstruction of the desired order.

- **Preprocessing.** Compute all control volume moments that will be needed in the least-squares problem of Equation 12.

- **Reconstruction.** For each control volume each time a function is reconstructed:

  1. Compute geometric weights, and construct the arrays needed for the data-independent least-squares problem of Equation 12.

  2. Solve the least-squares problem using Householder transformations. The solution algorithm should not destroy the original arrays and should return both the solution and the residual of the least-squares problem, along with information about how many derivatives were actually calculable.

  3. Using the residual of the least-squares problem, compute a data-dependent weight for each control volume in the stencil and multiply the appropriate row of the original least squares problem by this weight. Keep track of how many high weights there are, since this limits the number of derivatives that can be plausibly calculated.

  4. Solve the least-squares problem again. The derivatives computed give an ENO reconstruction when substituted into Equation 2.

4   Function Reconstruction

The reconstruction should be uniformly high-order accurate for smooth functions. To show this, we have reconstructed the function

$$u(x,y) = \cos(\pi x^2 + 4\pi y) \qquad (26)$$

on the square $[0,1] \times [0,1]$ using a series of unstructured triangular meshes ranging in size from 491 to 26651 vertices. The L_1 and L_2 norms of the error in reconstruction of this function are shown in Figure 2 for second- through fourth-order accuracy. Error norms are computed by using the difference between the analytic function and the reconstructed
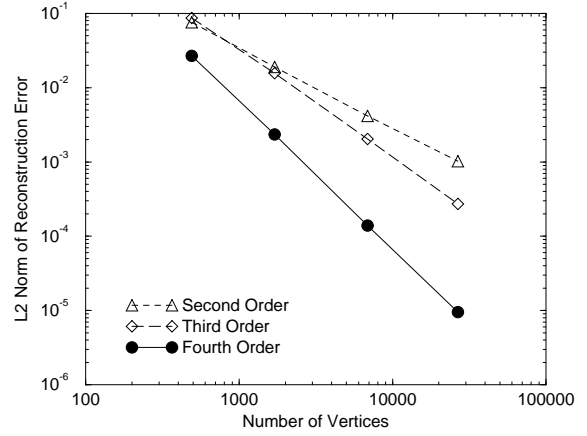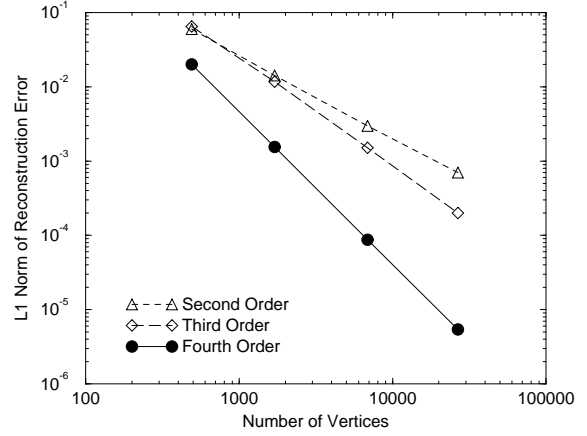
Convergence Order of Error Norms

Nominal	Norm	
Order	L_1	L_2
2	2.23	2.16
3	2.90	2.89
4	4.12	3.99

Figure 2: Convergence of k-Exact Reconstruction of a Smooth Function

function within each control volume. Sixth-order quadrature is used to compute the error norms in order to eliminate quadrature error in the computation of the norms. The accompanying table verifies that the expected asymptotic convergence rates are achieved.

The new reconstruction scheme was also tested for non-smooth function reconstruction in two dimen-
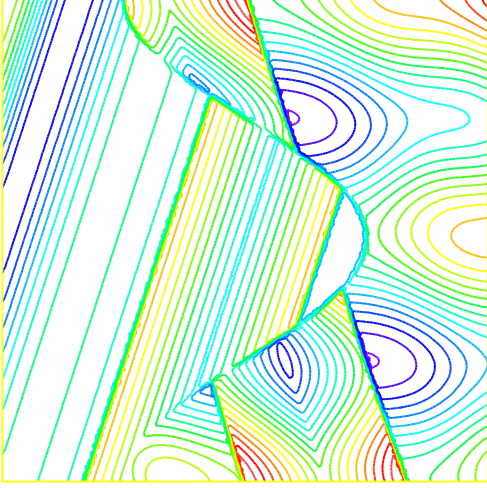
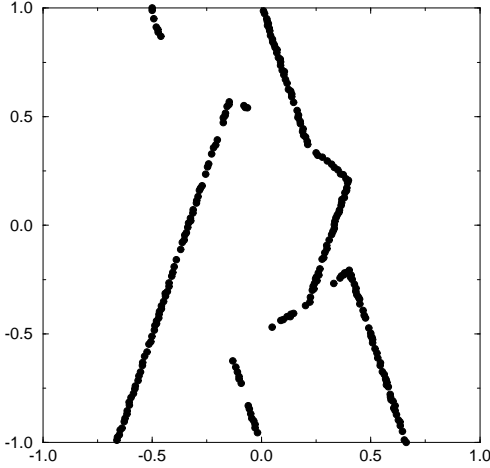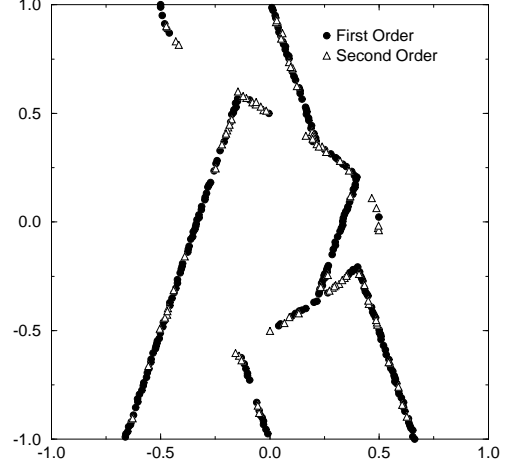Figure 3: Contours of Function Defined by Equation 27.

Figure 5: Control Volumes That Fail to Attain Third-Order Accuracy ($k = 2$)

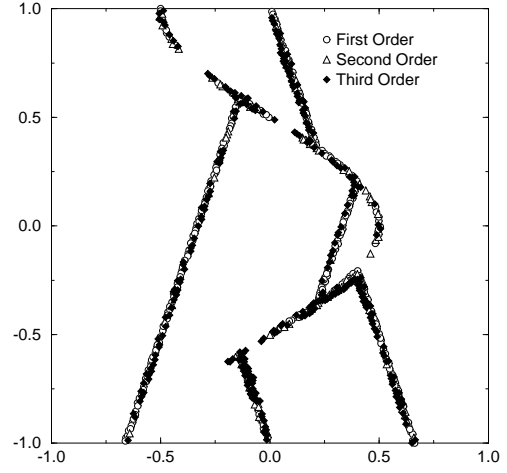Figure 4: Control Volumes That Fail to Attain Second-Order Accuracy ($k = 1$)

Figure 6: Control Volumes That Fail to Attain Fourth-Order Accuracy ($k = 3$)

sions. The function chosen is that of Abgrall [18].[‡]

$$u(x, y) = \begin{cases} f\left(x - \cot \sqrt{\frac{\pi}{2}} y\right) & x \leq \frac{\cos \pi y}{2} \\ f\left(x + \cot \sqrt{\frac{\pi}{2}} y\right) + \cos\left(2\pi y\right) & x > \frac{\cos \pi y}{2} \end{cases}$$
(27)

with

$$f(r) = \begin{cases} -r \sin\left(\frac{3\pi}{2} r^2\right) & r \leq -\frac{1}{3} \\ |\sin\left(2\pi r\right)| & |r| < \frac{1}{3} \\ 2r - 1 + \frac{1}{6} \sin\left(3\pi r\right) & r \geq \frac{1}{3} \end{cases}$$
(28)

Contour plots of this function are shown in Figure 3 Because the reconstruction scheme is k-exact (with or without data-dependent weighting), we know that

‡Several typographical errors in the definition of this function in [18] cause a mismatch with the plotted function there; the function shown here matches the plots in [18].

the accuracy of the reconstruction in smooth regions of the function will be of order $k + 1$. Norms of the error in the reconstruction are meaningless in this context, because the difference between the actual function and its reconstruction is guaranteed to be $\mathcal{O}(1)$ in control volumes that are crossed by a discontinuity. Instead, Figures 4–6 show the control volumes for which the nominal order of accuracy was not obtained on an isotropic triangular mesh with 26651 vertices for second through fourth order. The discontinuities in the function are clearly visible in these figures as control volumes with reduced reconstruction accuracy. In all control volumes away from the discontinuities, the nominal order of accuracy is attained. Table 1 shows the distribution of actual reconstruction accuracy for each case.

Table 1: Actual Accuracy of Reconstruction for Abgrall's Function

Nominal Order	Achieved Order			
	1	2	3	4
2	245	26406	—	—
3	233	82	26336	—
4	290	108	300	25953

5 Flow Solver Implementation

In addition to reconstruction, there are several other details in the construction of a high-order accurate flow solver which require careful attention.

5.1 Flux Quadrature

After the solution has been reconstructed from control-volume averages to a polynomial in each control volume, the second phase of the flow solution procedure is computation of a flux integral, or residual, for each control volume. This integration must be done to at least the same order of accuracy as the solution reconstruction to obtain high-order accuracy. In the present work, the integration is performed by Gaussian quadrature [19] around the boundary of each control volume. Gaussian quadrature has the property that an N-point quadrature along a line segment is $2N$-order accurate. Accordingly, first- and second-order accurate schemes ($k = 0, 1$) use $N = 1$, and third- and fourth-order schemes ($k = 2, 3$) use $N = 2$. Unfortunately, for the median dual this is not quite the full story, since the control volume boundary separating two adjacent volumes is not a single segment but two segments, each extending from the middle of an edge of the mesh to the centroid of a triangle. For first and second order, this is not a problem; a single point can still be used. Although in practice using the mid-edge seems adequate, in principle this point should be the centroid of the pair of line segments. For third and fourth order, two points on each part of the segment are, in principle, required. These options are illustrated in Figure 7. In both cases, the present work sticks to the letter of the law, using the quadrature points shown on the right side of the figure. As we shall see, computational time is dominated by reconstruction for high-order, so the additional flux computations are not a severe time penalty. At each quadrature point, the flux is evaluated using Roe's approximate Riemann solver [20].
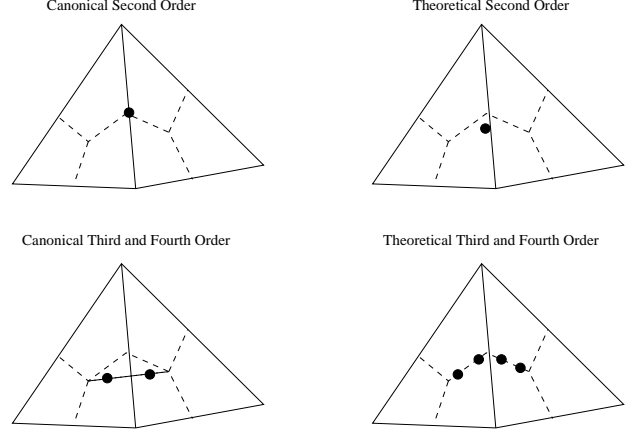

Figure 7: Choices for Gauss Integration Points for the Median Dual

5.2 Boundary Description and Implementation

A piecewise linear boundary description, as given by a polygonal input set, gives a second-order accurate representation of the shape of a smoothly curved boundary. For higher-order schemes, a more accurate boundary representation is required. The approach taken here is to specify, for each boundary segment, the inward normal at each end, as shown in Figure 8. This is equivalent to specifying slopes
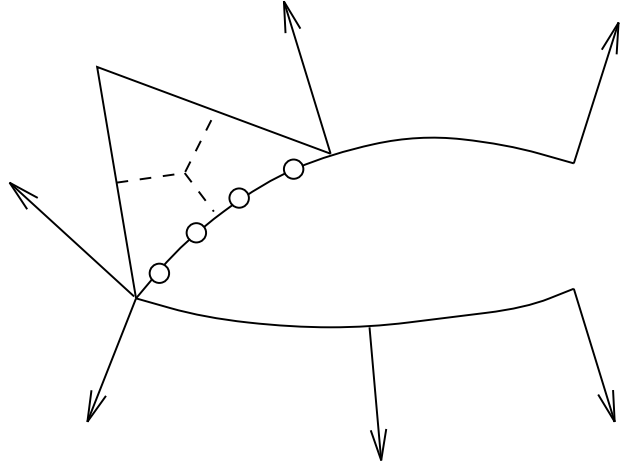

Figure 8: Schematic of High-Order Boundary Description

at the end of each segment and allows the flexibility to include sharp corners, because normals are defined edgewise rather than pointwise. This slope information is used to construct a piecewise cubic representation of the surface, which is fourth-order accurate for smoothly curved boundaries. This cubic representa-

tion is used to determine the Gauss integration data and control volume moments for control volumes on the boundary.

5.3 Computational Resources

Ultimately the question of practicality of high-order schemes will depend on trade-offs between accuracy and computational requirements. As preliminary data towards settling this question, requirements for CPU time and memory for the present implementation are tabulated here.

Table 2: Resource Requirements for High-Order Euler Solution on Two-Dimensional Unstructured Meshes

Resource Usage	Order of Accuracy		
	2	3	4
CPU Time (μsec / vertex / evaluation)[a]			
Reconstruction	255	1580	2180
Interior Flux Quad	130	573	649
Boundary Flux Quad	5.5	12.4	12.4
Memory (words / vertex)[b]			
Solution	$4f$	$4f$	$4f$
Derivatives	$8f$	$20f$	$36f$
Neighbor Information[c]	$7i$	$19i$	$19i$
Gauss Point Locations[d]	$6f$	$24f$	$24f$
Gauss Point Normals[‡]	$6f$	$12f$	$12f$
Gauss Weights[‡]	$3f$	$6f$	$6f$
Total	$27f$ $+7i$	$84f$ $+19i$	$100f$ $+19i$

[a] On a 110 MHz SPARC 5

[b] f = floating point, i = integer

[c] Average for interior vertices

[d] Assuming three times as many edges as vertices

6 Flow Solutions

6.1 Supersonic Vortex Flow

A smooth flow was calculated to validate the accuracy of the high-order boundary shape definition and flux quadrature. The flow chosen was a supersonic vortex flow in a quarter-circular annulus. This is an isentropic flow in which the velocity is inversely proportional to radius and the density is given by

$$\rho = \rho_i \left[1 + \frac{\gamma - 1}{2} M_i^2 \left(1 - \frac{r_i^2}{r^2} \right) \right]^{\frac{1}{\gamma - 1}}, \qquad (29)$$

where the subscript i denotes quantities at the inner boundary. For this case, r_i was chosen to be 2, $r_o = 3$, and $M_i = 2$. Four isotropic triangular meshes were
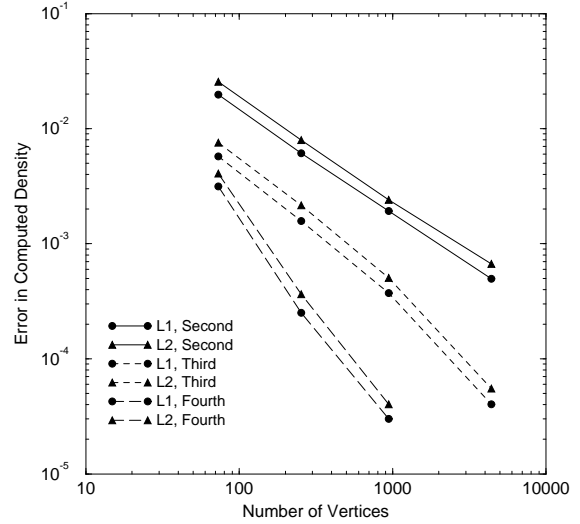
Convergence Order of Error Norms

Nominal Order	Norm	
	L_1	L_2
2	1.79	1.78
3	2.88	2.87
4	3.64	3.61

Figure 9: Error in Density for Supersonic Vortex Flow

used for this case, containing 73, 253, 941, and 4398 vertices. Error norms are computed from the solution in the same way as for reconstruction. Figure 9 shows the L_1 and L_2 norms of the error in density for this problem, and the accompanying table indicates the asymptotic order of accuracy achieved.

6.2 Transonic Airfoil Flow

To verify that the scheme behaves well for flows with weak shocks, AGARD test case 1 [21] was computed on a mesh with 4156 vertices, shown in Figure 10. Because the current scheme is an ENO scheme, we are interested not only in the solutions but also in the convergence behavior, to verify that it is possible to converge to machine zero. Figure 11 shows the surface pressure coefficients for this case for second- and third-order accuracy. There is little visible difference in the solutions at this scale. Each solution shows a mild oscillation near the shock. Of note also is the behavior near the leading edge stagnation point. In
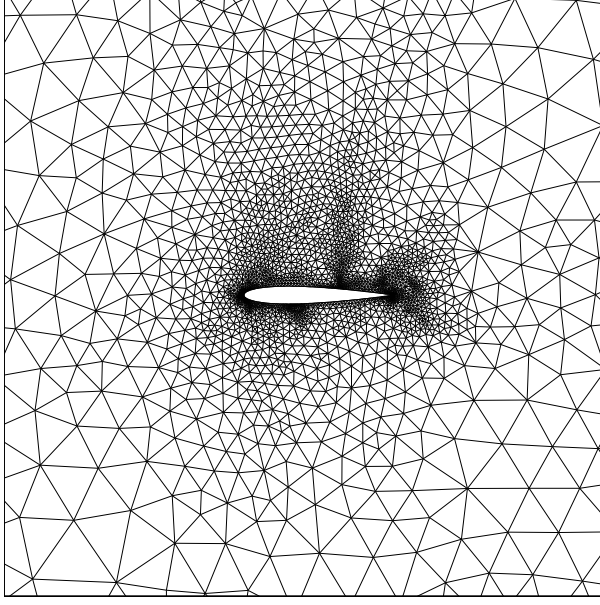
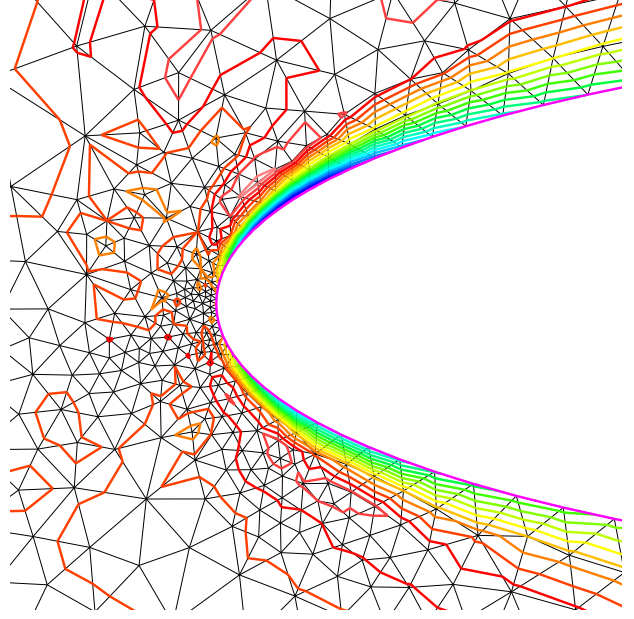Figure 10: Mesh for AGARD Test Case 1 (4156 vertices)

Figure 11: Surface Pressure Coefficient for AGARD Test Case 1

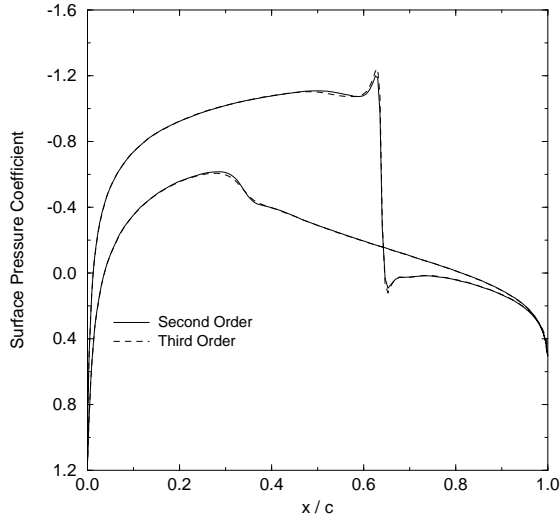Figure 12: Stagnation Pressure Coefficient Near Leading Edge for AGARD Test Case 1 (Second Order)

Figure 13: Stagnation Pressure Coefficient Near Leading Edge for AGARD Test Case 1 (Second Order)

this region, stagnation pressure loss is often relatively high because of poor resolution of the rapidly turning flow. Figures 12 and 13 demonstrate a marked improvement in the losses at the leading edge when going from second to third order. In each figure, contour levels are separated by 0.04 and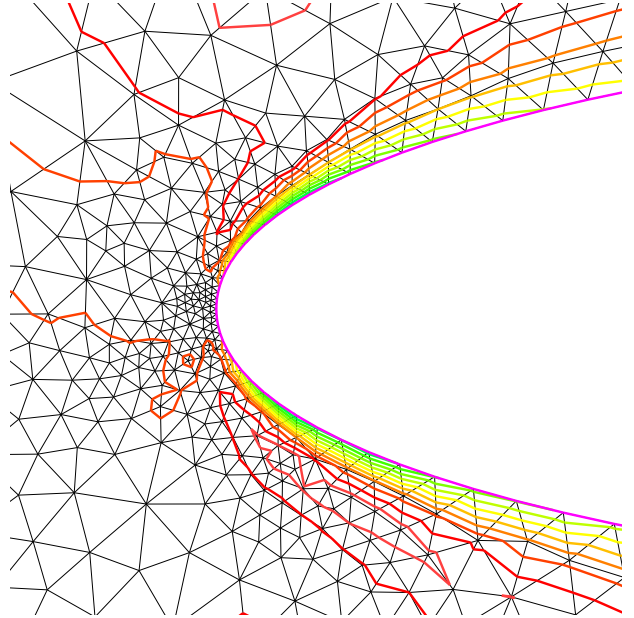 the contours away from the body are at 0 or ±0.04. The peak value for second order is about 0.072, while for third order it is about 0.036.

Figure 14 shows the convergence history for these cases. Multigrid W-cycles were used in conjunction with local time step and a three-stage time-stepping
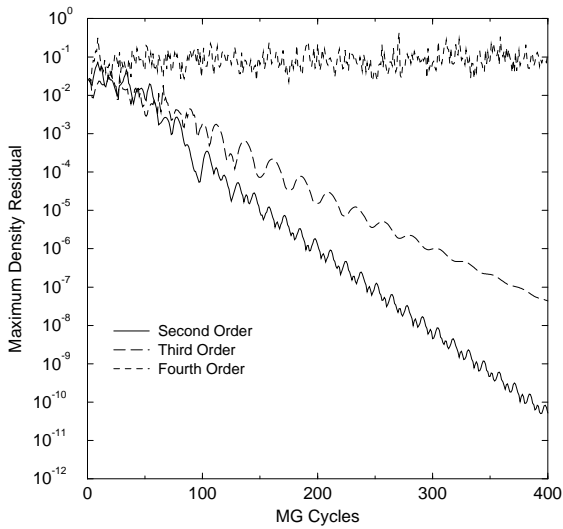
Figure 14: Convergence Histories, AGARD Test Case 1

Figure 15: Scramjet Geometry

Figure 16: Scramjet Density Contours

scheme. No serious effort has been made to optimize the multistage scheme or the CFL number. The figure shows that convergence for the third-order scheme is not as good as for second order, but both converge well with none of the hang-ups often seen with stencil-searching ENO schemes. The fourth-order scheme does hang up, with oscillations in shock position and shape being the culprit. Further study is needed to eliminate this problem.

6.3 Scramjet Configuration

The scramjet configuration introduced by Kumar [22] was computed at M=5, $\alpha = 0$, solely as a robustness demonstration. The geometry for this case is shown in Figure 15. A nearly uniform, isotropic triangular mesh with 8841 vertices was generated. Figure 16 shows density contours for a second-order accurate solution of this problem. Much of the detail of the flow is missing because of poor resolution (for example, the throat is only nine cells across), but the broad outlines of the shock reflections and interactions are present. Clearly, local refinement would be of tremendous benefit in resolving this flow.

7 Conclusions

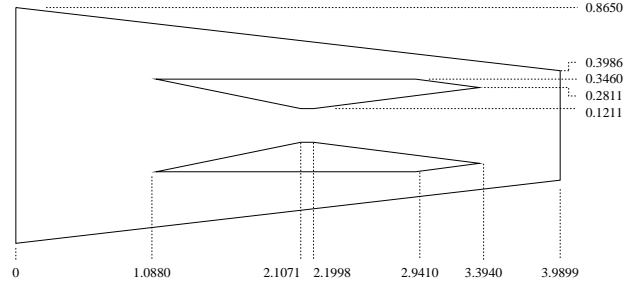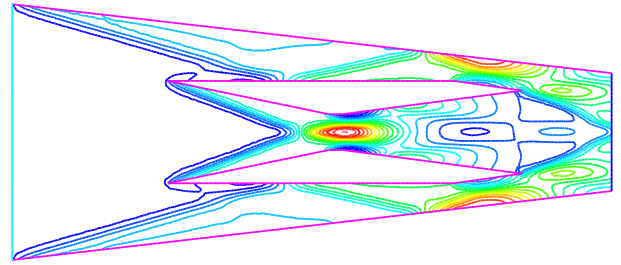This article has demonstrated the feasibility of computing high-order accurate solutions to the Euler equations on unstructured triangular meshes using an ENO scheme. Reconstruction accuracy for smooth functions has been verified, and the reconstruction scheme behaves gracefully near function discontinuities. Accuracy for smooth flows has been established by comparing computation with an analytic solution. The scheme has been shown to be capable of converging to machine zero. Finally, the scheme's ability to handle complex, high Mach number flows robustly has been demonstrated.

A number of open questions remain.

- Extension to a three-dimensional flow solver will likely require switching to a cell-centered scheme because of the complex shape of vertex-centered control volumes. Might it also be advantageous to use a cell-centered scheme in two dimensions?

- In smooth regions of the flow, data-dependent reconstruction is unnecessary; an excellent representation of the solution is provided by the data-independent reconstruction. Can the scheme recognize and exploit this feature without causing convergence to hang up by switching?

- In very flat regions of the flow, the use of fourth-order accuracy is, in a practical sense, overkill. Second- or even first-order accuracy may be sufficient to represent the solution. How must a p-refinement scheme be designed to choose optimal accuracy locally?

- Some convergence and robustness questions re-

main. Certain cases violate positivity, and convergence rates are not particularly good.

References

[1] van Leer, B., "Towards the Ultimate Conservative Difference Scheme. V. A Second-Order Sequel to Godunov's Method," *Journal of Computational Physics*, vol. 32, pp. 101–136, 1979.

[2] Harten, A. and Osher, S., "Uniformly High-Order Accurate Nonoscillatory Schemes," *SIAM Journal on Numerical Analysis*, vol. 24, pp. 279–309, Apr. 1987.

[3] Harten, A., Osher, S., Engquist, B., and Chakravarthy, S. R., "Some Results on Uniformly High-Order Accurate Essentially Non-Oscillatory Schemes," *Applied Numerical Mathematics*, vol. 2, pp. 347–377, 1986.

[4] Harten, A., Enquist, B., Osher, S., and Chakravarthy, S. R., "Uniformly High Order Accurate Essentially Non-oscillatory Schemes, III," *Journal of Computational Physics*, vol. 71, pp. 231–303, Aug. 1987.

[5] Shu, C.-W. and Osher, S., "Efficient Implementation of Essentially Non-oscillatory Shock-Capturing Schemes, II," *Journal of Computational Physics*, vol. 83, pp. 32–78, 1989.

[6] Shu, C.-W., Zang, T. A., Erlebacher, G., Whitaker, D., and Osher, S., "High-order ENO Schemes Applied to Two- and Three-Dimensional Compressible Flow," *Applied Numerical Mathematics*, vol. 9, no. 1, pp. 45–71, 1992.

[7] Casper, J., *An Extension of Essentially Non-Oscillatory Shock Capturing Schemes to Multi-Dimensional Systems of Conservation Laws*. PhD thesis, Old Dominion University, Dec. 1990.

[8] Godfrey, A. G., Mitchell, C. R., and Walters, R. W., "Practical Aspects of Spatially High-Order Accurate Methods," *AIAA Journal*, vol. 31, pp. 1634–1642, Sept. 1993.

[9] Liu, X.-D., Osher, S., and Chan, T., "Weighted Essentially Non-oscillatory Schemes," *Journal of Computational Physics*, vol. 115, pp. 200–212, 1994.

[10] Jiang, G.-S. and Shu, C.-W., "Efficient Implementation of Weighted ENO Schemes," *Journal of Computational Physics*, vol. 126, pp. 202–228, June 1996.

[11] Durlofsky, L. J., Enquist, B., and Osher, S., "Triangle Based Adaptive Stencils for the Solution of Hyperbolic Conservation Laws," *Journal of Computational Physics*, vol. 98, pp. 64–73, Jan. 1992.

[12] Abgrall, R., "On Essentially Non-oscillatory Schemes on Unstructured Meshes: Analysis and Implementation," *Journal of Computational Physics*, vol. 114, no. 1, pp. 45–58, 1994.

[13] Barth, T. J., "Recent Developments in High Order K-Exact Reconstruction on Unstructured Meshes." AIAA paper 93-0668, Jan. 1993.

[14] Venkatakrishnan, V., "On the Accuracy of Limiters and Convergence to Steady-State Solutions." AIAA paper 93-0880, Jan. 1993.

[15] Jameson, A., "Artificial Diffusion, Upwind Biasing, Limiters and their Effect on Accuracy and Multigrid Convergence in Transonic and Hypersonic Flows." AIAA paper 93-3359-CP, July 1993.

[16] Ollivier-Gooch, C. F., "Quasi-ENO Schemes for Unstructured Meshes Based on Unlimited Data-Dependent Least-Squares Reconstruction," *Journal of Computational Physics*. To appear.

[17] Golub, G. H. and van Loan, C. F., *Matrix Computations*. Baltimore, Maryland: The Johns Hopkins University Press, 1983.

[18] Abgrall, R., "Design of an Essentially Non-oscillatory Reconstruction Procedure on Finite-Element Type Meshes." ICASE Report No. 91-84, NASA Langley Research Center, 1991. NASA CR 189574.

[19] Stroud, A. H. and Secrest, D., *Gaussian Quadrature Formulas*. Englewood Cliffs, N.J.: Prentice-Hall, 1966.

[20] Roe, P. L., "Approximate Riemann Solvers, Parameter Vectors, and Difference Schemes," *Journal of Computational Physics*, vol. 43, pp. 357–372, 1981.

[21] AGARD Fluid Dynamics Panel, *Test Cases for Inviscid Flow Field Methods*. AGARD, May 1985. AGARD Advisory Report AR-211.

[22] Kumar, A., "Numerical Analysis of the Scramjet-Inlet Flow Field by Using Two-Dimensional Navier-Stokes Equations," Technical Paper 1940, NASA, December 1981.